Optimized detection of shear peaks in weak lensing maps

Laura Marian,[1]⋆ Robert E. Smith,[1,2] Stefan Hilbert[1,3,4] and Peter Schneider[1]

[1]*Argelander-Institute for Astronomy, Auf dem Hügel 71, D-53121 Bonn, Germany*
[2]*Institute for Theoretical Physics, University of Zurich, Zurich CH 8037, Switzerland*
[3]*Kavli Institute of Particle Astrophysics and Cosmology (KIPAC), Stanford University, 452 Lomita Mall, Stanford, CA 94305, USA*
[4]*SLAC National Accelerator Laboratory, 2575 Sand Hill Road, M/S 29, Menlo Park, CA 94025, USA*

ABSTRACT

We present a new method to extract cosmological constraints from weak lensing (WL) peak counts, which we denote as 'the hierarchical algorithm'. The idea of this method is to combine information from WL maps sequentially smoothed with a series of filters of different size, from the largest down to the smallest, thus increasing the cosmological sensitivity of the resulting peak function. We compare the cosmological constraints resulting from the peak abundance measured in this way and the abundance obtained by using a filter of fixed size, which is the standard practice in WL peak studies. For this purpose, we employ a large set of WL maps generated by ray tracing through N-body simulations, and the Fisher matrix formalism. We find that if low signal-to-noise ratio (S/N) peaks are included in the analysis (S/N $\sim$ 3), the hierarchical method yields constraints significantly better than the single-sized filtering. For a large future survey such as *Euclid* or Large Synoptic Survey Telescope, combined with information from a cosmic microwave background experiment like *Planck*, the results for the hierarchical (single-sized) method are $\Delta n_{\rm s} = 0.0039\,(0.004)$, $\Delta\Omega_{\rm m} = 0.002\,(0.0045)$, $\Delta\sigma_8 = 0.003\,(0.006)$ and $\Delta w = 0.019\,(0.0525)$. This forecast is conservative, as we assume no knowledge of the redshifts of the lenses, and consider a single broad bin for the redshifts of the sources. If only peaks with S/N $\geq$ 6 are considered, then there is little difference between the results of the two methods. We also examine the statistical properties of the hierarchical peak function: Its covariance matrix has off-diagonal terms for bins with S/N $\leq$ 6 and aperture mass of $M < 3 \times 10^{14}\,h^{-1}\,{\rm M}_\odot$, the higher bins being largely uncorrelated and therefore well described by a Poisson distribution.

Key words: cosmology: theory – large-scale structure of Universe.

1 INTRODUCTION

For more than a decade, weak gravitational lensing (WL) has been considered a powerful probe for testing cosmology due to its potential to map the three-dimensional (3D) matter distribution of the Universe in an unbiased way, independent of baryonic matter tracers.

Several surveys have already demonstrated the ability of WL to constrain the cosmological model through cosmic shear measurements, e.g. the Cerro Tololo Inter-American Observatory (CTIO) Lensing Survey (Jarvis et al. 2003, 2006), the Garching–Bonn Deep Survey (GaBoDS; Hetterscheidt et al. 2007) and the Canada–France–Hawaii Telescope Legacy Survey (CFHTLS; Hoekstra et al. 2006; Semboloni et al. 2006).

Among the WL probes are shear peaks, regions of high signal-to-noise ratio (S/N) in shear maps that can be produced by individual clusters or by the alignment of several smaller objects on the line of sight. The abundance of shear peaks is as sensitive to cosmology as the cluster mass function (Marian, Smith & Bernstein 2009, 2010; Kratochvil, Haiman & May 2010; Kratochvil et al. 2011; Yang et al. 2011). Clusters are one of the four most promising tools to measure dark energy (Albrecht et al. 2006), together with supernova surveys, baryonic acoustic oscillations and WL surveys. Therefore, the WL peak function is equally promising in principle. There are two major advantages of WL peaks over clusters: (i) WL peaks will come for free with any future lensing survey; (ii) one can very reliably calibrate the abundance of peaks with cold dark matter (CDM) simulations and proceed with direct comparisons to data measurements, thus bypassing the thorny issue of the mass–observable relation. Shear peak signals need not be translated into virial masses in order to be able to extract cosmological information from their abundance (Dietrich & Hartlap 2010). A disadvantage is the absence of an analytical framework for the WL peaks (though see the recent work of Maturi et al. 2010).

Detections of shear peaks in WL data are exemplified in the works of Dahle (2006), Schirmer et al. (2007), Bergé et al. (2008) and Abate et al. (2009). However, the exploration of the shear signal

of clusters has been focused mostly on mass determination, as for instance in the recent work of Okabe et al. (2010) and Israel et al. (2010).

Since the introduction of the aperture mass by Schneider (1996), there have been many studies of filters optimal for peak detection and of the impact of large-scale structure (LSS) projections on cluster mass reconstructions (e.g. Hoekstra 2001; Metzler, White & Loken 2001; Clowe, De Lucia & King 2004; Hamana, Takada & Yoshida 2004; Hennawi & Spergel 2005; Maturi et al. 2005; Tang & Fan 2005; Marian et al. 2010; Becker & Kravtsov 2011; Gruen et al. 2011). The general agreement is that cluster masses derived from WL measurements are affected by both correlated and uncorrelated LSS projections, as well as by departures of the density profiles of real clusters from the assumed spherical models. These effects cause scatter and bias in the predicted and measured S/N of the clusters. Nonetheless, WL mass reconstructions retain the attractive feature of being able to rely on numerical simulations for accurate predictions of such biases.

In this paper we address a more general question related to the abundance of shear peaks. Given the upcoming WL surveys such as the Kilo-Degree Survey (KiDS; Kuijken 2010), the Dark Energy Survey (DES; The Dark Energy Survey Collaboration 2005), the Large Synoptic Survey Telescope (LSST) survey (LSST Science Collaborations et al. 2009) or the *Euclid* survey (The Euclid Collaboration 2011), it will be possible to measure the shear peak function: what is the optimal way to do this?

The standard approach to peak detection is as follows: a given shear map is smoothed with a given filter function; in the smoothed map, one looks for points of local maximum which have S/N higher than a certain chosen threshold value, and one selects these points as 'peaks'. This procedure is dependent on the filter used. There have been many studies on the shape of filters that maximize the S/N assuming certain shapes for the peak signal and various types of noise such as shape noise or projection noise (e.g. Hennawi & Spergel 2005; Maturi et al. 2005; Gruen et al. 2011).

Less attention has been directed towards the size of filters. Indeed in most studies, the peak abundances are measured using a single-sized filter (e.g. Hamana et al. 2004; Dietrich & Hartlap 2010), though it is clear that each size will lead to a different peak function. For a different approach using wavelets, see Pires et al. (2009). Here we propose a method that we call 'hierarchical algorithm': a shear map is smoothed with several filters of the same shape but different size, from the largest to the smallest. We show that by taking into account the extended information from such multiscale filtering, one can assign in the context of an assumed halo paradigm, e.g. the Navarro, Frenk & White (1997) (NFW) model, a unique S/N and (redshift-dependent) mass to the detected peaks. We use the Fisher matrix formalism and a large set of simulated WL maps to

show that the cosmological constraints derived from the hierarchical peak function are much improved compared to those obtained using a filter of the same shape but only one size.

The paper is structured as follows. In Section 2, we present the *N*-body simulations and the ray tracing performed to generate the WL maps employed in this study. In Section 3, we explain the hierarchical scheme and the filter that we adopt. The results of this work are presented in Section 4, along with a WL-peaks Fisher forecast for surveys like *Euclid* and LSST, the first to be obtained from simulation measurements. In Section 5, we summarize and conclude.

2 NUMERICAL SIMULATIONS AND RAY TRACING

We generated WL maps from ray tracing through *N*-body simulations. We used eight simulations which are part of a larger suite performed on the zBOX-2 and zBOX-3 supercomputers at the University of Zürich. For all realizations 11 snapshots were output between redshifts $z = [0, 2]$; further snapshots were at redshifts $z = \{3, 4, 5\}$. We shall refer to these simulations as the zHORIZON simulations, and they were described in detail in Smith (2009).

Each of the zHORIZON simulations was performed using the publicly available GADGET-2 code (Springel 2005), and followed the non-linear evolution under gravity of $N = 750^3$ equal-mass particles in a comoving cube of length $L_{sim} = 1500\,h^{-1}$ Mpc; the softening length was $l_{soft} = 60\,h^{-1}$ kpc. The cosmological model was similar to that determined by the *Wilkinson Microwave Anisotropy Probe* (*WMAP*) experiment (Komatsu et al. 2009). We refer to this cosmology as the fiducial model. The transfer function for the simulations was generated using the publicly available CMBFAST code (Seljak & Zaldarriaga 1996), with high sampling of the spatial frequencies on large scales. Initial conditions were set at redshift $z = 50$ using the serial version of the publicly available 2LPT code (Scoccimarro 1998; Crocce, Pueblas & Scoccimarro 2006). Table 1 summarizes the cosmological parameters that we simulated and Table 2 summarizes the numerical parameters used.

For the Fisher matrix study of peak counts, we employed another series of simulations. Each of the new set was identical in every way to the fiducial model, except that we have varied one of the cosmological parameters by a small amount. For each new set we have generated four simulations, matching the random realization of the initial Gaussian field with the corresponding one from the fiducial model. The four parameter variations were $\{n \rightarrow (0.95, 1.05), \sigma_8 \rightarrow (0.7, 0.9), \Omega_m \rightarrow (0.2, 0.3), w \rightarrow (-1.2, -0.8)\}$, and we refer to each of the sets as zHORIZON-V1a,b,...,zHORIZON-V4a,b, respectively. The details are summarized in Tables 1 and 2.

Table 1. zHORIZON cosmological parameters. Columns are the following: density parameters for matter, dark energy and baryons; the equation of state parameter for the dark energy; normalization and primordial spectral index of the power spectrum; dimensionless Hubble parameter.

Cosmological parameters	Ω_m	Ω_{DE}	Ω_b	w	σ_8	n	H_0 (km s^{-1} Mpc^{-1})
zHORIZON-I	0.25	0.75	0.04	-1	0.8	1.0	70.0
zHORIZON-V1a/V1b	0.25	0.75	0.04	-1	0.8	0.95/1.05	70.0
zHORIZON-V2a/V2b	0.25	0.75	0.04	-1	0.7/0.9	1.0	70.0
zHORIZON-V3a/V3b	0.2/0.3	0.8/0.7	0.04	-1	0.8	1.0	70.0
zHORIZON-V4a/V4b	0.25	0.75	0.04	$-1.2/-0.8$	0.8	1.0	70.0

Table 2. zHORIZON numerical parameters. Columns are the following: number of particles, box size, particle mass, force softening, number of realizations and total simulated volume.

Simulation parameters	N_{part}	L_{sim} (h^{-1} Mpc)	m_p (h^{-1} M$_\odot$)	l_{soft} (h^{-1} kpc)	N_{ensemb}	V_{tot} (h^{-3} Gpc^3)
zHORIZON-I	750^3	1500	5.55×10^{11}	60	8	27
zHORIZON-V1, -V2, -V4	750^3	1500	5.55×10^{11}	60	4	13.5
zHORIZON-V3a	750^3	1500	4.44×10^{11}	60	4	13.5
zHORIZON-V3b	750^3	1500	6.66×10^{11}	60	4	13.5

For the WL simulations, we considered a survey similar to *Euclid* (The Euclid Collaboration 2011) and to LSST (LSST Science Collaborations et al. 2009), with an rms $\sigma_\gamma = 0.3$ for the intrinsic image ellipticity, a source number density $\bar{n} = 40$ arcmin^{-2} and a redshift distribution of source galaxies given by

$$\mathcal{P}(z) = \mathcal{N}(z_0, \beta) \, z^2 \exp[-(z/z_0)^\beta], \quad (1)$$

where the normalization constant $\mathcal{N}$ insures that the integral of the source distribution over the source redshift interval is unity. If this interval extended to infinity, then the normalization could be written analytically as $\mathcal{N} = 3/(z_0^3 \, \Gamma[(3 + \beta)/\beta])$. There is a small difference between this value and what we actually used, due to the fact that we considered a source interval of [0, 3]. We took $\beta = 1.5$, and required that the median redshift of this distribution be $z_{med} = 0.9$, which fixed $z_0 \approx 0.64$, and gave a mean of $z_{mean} = 0.95$.

From each N-body simulation we generated 16 independent fields of view. Each field had an area of 12×12 deg^2 and was tiled by 4096^2 pixels, yielding an angular resolution $\theta_{pix} = 10$ arcsec. For each variational model, the total area was of ≈ 9000 deg^2, while for the fiducial model it was of ≈ 18000 deg^2. The effective convergence κ in each pixel was calculated by tracing a light ray back through the simulation with a multiple-lens-plane ray-tracing algorithm (Hilbert et al. 2007a, 2009). Gaussian shape noise with variance $\sigma_\gamma^2/(\bar{n} \, \theta_{pix}^2)$ was then added to each pixel, creating a realistic noise level and correlation in the filtered convergence field (Hilbert, Metcalf & White 2007b). We keep the shape noise configuration fixed for each field in different cosmologies, in order to minimize its impact on the comparisons of the peak abundances measured for each cosmology.

3 SMOOTHING WEAK LENSING MAPS

3.1 A matched filter

To find peaks in WL maps, we smooth the latter with an aperture-mass filter (Schneider 1996; Schneider et al. 1998). The smoothed convergence map is a convolution between the filter function and the κ/γ field of our simulations:

$$M_{ap}(\boldsymbol{\theta}_0) = \int d^2\theta \, U(\boldsymbol{\theta}_0 - \boldsymbol{\theta}) \kappa(\boldsymbol{\theta}) = \int d^2\theta \, Q(\boldsymbol{\theta}_0 - \boldsymbol{\theta}) \gamma(\boldsymbol{\theta}), \quad (2)$$

where κ is the convergence, γ is the tangential shear field and U and Q are aperture filters for convergence and shear, respectively. $\boldsymbol{\theta}_0$ is an arbitrary point. Aperture-mass filters are compensated, which for a spherically symmetric function can be expressed through the equation

$$\int_0^{\theta_A} d\theta \, \theta \, U(\theta) = 0, \quad (3)$$

where θ_A is the compensation radius. In the presence of the ellipticity noise of the source galaxies, it can be shown that an optimal and compensated filter is given by

$$U(\theta) = \mathcal{C} \, \frac{\kappa_m(\theta) - \bar{\kappa}_m(\theta_A)}{\sigma_\gamma^2/\bar{n}}, \quad (4)$$

where $\mathcal{C}$ is an arbitrary normalization constant, κ_m is the adopted model for the convergence profile of peaks, i.e. NFW or similar, and $\sigma_\gamma^2/\bar{n}$ is the shape noise variance per ellipticity component. The mean convergence inside a radius θ is defined by $\bar{\kappa}(\theta) = 2/\theta^2 \int_0^\theta d\theta' \, \theta' \kappa(\theta')$. The analogue filter function for the shear field is given by

$$Q(\theta) = \mathcal{C} \, \frac{\gamma_m(\theta)}{\sigma_\gamma^2/\bar{n}}, \quad (5)$$

where γ_m is the assumed tangential shear model of the peaks. Under the assumption that the shape noise is the dominant source of noise in the measurements, this filter is optimal because it maximizes the S/N at the location of a peak with the convergence/shear profile κ_m/γ_m. From equations (2) and (4), the S/N can be written as

$$S/N(\boldsymbol{\theta}_0) = \sqrt{\frac{\bar{n}}{\sigma_\gamma^2}} \frac{\int d^2\theta \, [\kappa_m(\theta) - \bar{\kappa}_m(\theta_A)] \kappa(\boldsymbol{\theta}_0 - \boldsymbol{\theta})}{\sqrt{\int d^2\theta \, [\kappa_m(\theta) - \bar{\kappa}_m(\theta_A)]^2}}, \quad (6)$$

or in terms of the shear

$$S/N(\boldsymbol{\theta}_0) = \sqrt{\frac{\bar{n}}{\sigma_\gamma^2}} \frac{\int d^2\theta \, \gamma_m(\theta) \, \gamma(\boldsymbol{\theta}_0 - \boldsymbol{\theta})}{\sqrt{\int d^2\theta \, \gamma_m^2(\theta)}}. \quad (7)$$

Note that the S/N *does not* depend on the arbitrary normalization constant $\mathcal{C}$.

Although we do not make a comparison between peaks and clusters, and indeed do not use any information on the simulation haloes in this study, our choice of $\mathcal{C}$ provides insight into the haloes that generate the peaks (though of course not all the peaks will correspond to a halo). If $\boldsymbol{\theta}_0$ denotes the location of a peak formed by a halo of mass M_m, redshift z_m and profile $\kappa(\theta) = \kappa_m(\theta; M_m, z_m)$, then we require that the amplitude of the smoothed map at the location of this peak be exactly M_m: $M_{ap}(\boldsymbol{\theta}_0) = M_m$. In this case, $\mathcal{C}$ is given by (Marian & Bernstein 2006)

$$\mathcal{C}(M_m) = \sigma_\gamma^2/\bar{n} \, \frac{M_m}{\int d^2\theta \, \kappa_m^2(\theta) - \pi \theta_A^2 \bar{\kappa}_m^2(\theta_A)}. \quad (8)$$

In the above equation, $\kappa_m(\theta) = \kappa_m(\theta; M_m, z_m)$ and it is assumed that the radial integral has an upper limit of θ_A. The latter applies also to equations (6), (7) and (10). Note that for the shear filter the normalization is the same, since

$$2\pi \int_0^{\theta_A} d\theta \, \theta \, \kappa_m^2(\theta) - \pi \theta_A^2 \, \bar{\kappa}_m^2(\theta_A) = 2\pi \int_0^{\theta_A} d\theta \, \theta \, \gamma_m^2(\theta). \quad (9)$$

Our analysis was performed on convergence maps, and so in the following, we shall focus on the latter. Inserting equations (4) and (8) into equation (2), we write down the amplitude of the smoothed map for our particular choice of matched aperture filter:

$$\begin{aligned} M_{ap}(\boldsymbol{\theta}_0) &= M_m \frac{\int d^2\theta \, [\kappa_m(\theta) - \bar{\kappa}_m(\theta_A)] \kappa(\boldsymbol{\theta}_0 - \boldsymbol{\theta})}{\int d^2\theta \, \kappa_m^2(\theta) - \pi \theta_A^2 \bar{\kappa}_m^2(\theta_A)} \\ &= \sqrt{\mathcal{C}(M_m)} \, S/N(\boldsymbol{\theta}_0). \end{aligned} \quad (10)$$

Within the validity bounds of our model, i.e. the peak is indeed generated by an NFW halo of that mass and redshift, equation (10) represents an unbiased estimator for mass.

Finally, we assume a relation between the model mass M_m and the compensation radius: we take the latter to be the angular scale subtended by the virial radius of a halo with mass M_m, redshift z_m and convergence profile κ_m:

$$\theta_A = R_{\rm vir}(M_m, z_m)/D_A(z_m), \tag{11}$$

where $D_A(z_m)$ is the angular diameter distance to z_m. This choice enables us to connect the 'size' of the filter, i.e. the aperture radius, with the 'mass' of the filter M_m, using the standard relation between mass and virial radius provided by models of structure formation, such as NFW for instance. Given the source distribution in equation (1), we take $z_m = 0.3$. This is just a clarification of what we mean by size and mass of the filter, all the necessary details will be provided in Section 3.3.

3.2 Hierarchical filtering

We shall now describe our method to detect shear peaks and assign them masses and S/N. This was already implemented in our previous works (Marian et al. 2009, 2010, 2011).

As mentioned in Section 3.1, smoothed maps are obtained by convolving the convergence field with a filter, e.g. equation (2). Peaks are detected as local maxima in the smoothed maps, i.e. points with amplitude higher than that of their eight neighbours, where the amplitude is given by equation (2), or in our particular case, by equation (10). Medium or large peaks will still be local maxima even when smoothed with filters of size much larger or smaller than the peak radius. However, the S/N and amplitude associated with the peak will be quite different for a range of filter sizes spanning one to two orders of magnitude. Therefore, there is some degree of arbitrariness when trying to classify the abundance of WL peaks in terms of their S/N or amplitude: the answer will depend on the filter size. Furthermore, if the peaks are small, then a large filter may render them quite indistinguishable from spurious shape–noise peaks. The strengths of our top-down approach are the following.

(i) It uses filters of several sizes, which will increase the scale range of the detected peaks and therefore the cosmological information of the peak counts.

(ii) It uses an interpolation scheme for the results of the smoothing with each filter to accurately establish a unique value for the S/N and amplitude $M_{\rm ap}$ of each peak. Thus the ambiguity of classifying peaks in terms of their S/N is removed, and one obtains a 'general' peak function, as opposed to a different peak function for each filter size employed in smoothing.

The concrete steps that we take are as follows. We smooth the maps with a sequence of filters of different sizes (masses), in a hierarchical fashion, from the largest to the smallest size. The purpose is to determine the 'mass' of the peaks, i.e. the filter size which matches best the size of the peaks:

$$M_{\rm ap}(\boldsymbol{\theta}_0) = M_m, \tag{12}$$

where $\boldsymbol{\theta}_0$ denotes the location of a detected peak. For each filter i in the sequence, the peaks are selected so that (a) $M_{\rm ap}^i \geq M_m^i$; (b) $S/N^i \geq (S/N)_{\rm min}$, where M_m^i is the size of the filter. $M_{\rm ap}^i$ and S/N^i are the aperture mass and S/N defined in equations (6) and (10) corresponding to this particular filter, and we choose $(S/N)_{\rm min} = 3$ as a detection threshold.
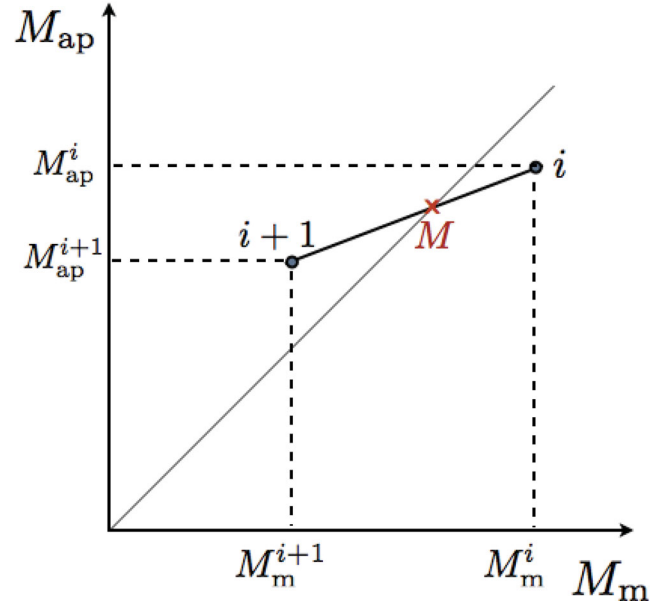

Figure 1. Matching between the filter and peak profiles in the hierarchical method. The larger filter M_m^i yields an aperture mass $M_{\rm ap}^i < M_m^i$ while the next filter in the sequence, of smaller size M_m^{i+1}, gives an aperture mass $M_{\rm ap}^{i+1} > M_m^{i+1}$. The solution M to equation (12) is found through interpolation to be equation (13). We take this to be the 'true' mass of the peak.

Equation (12) is not likely to be satisfied by any particular filter in the sequence, hence we find its solution by interpolating between the results of smoothing with different filters in the sequence. This is illustrated in Fig. 1. Suppose there is a peak of true mass M and S/N (true according to the assumed model). Then there will be two consecutive filters in the sequence, i and $i + 1$, for which the following relations are true:

$$M_m^i > M_{\rm ap}^i > M > M_{\rm ap}^{i+1} > M_m^{i+1}, \; S/N^i > S/N > S/N^{i+1}.$$

Since the aperture mass of the peak obtained from consecutive filters varies gently with the size of the filter, we can use linear interpolation to write down the solution for the true mass, i.e. the solution of equation (12):

$$M = \frac{M_m^i M_{\rm ap}^{i+1} - M_m^{i+1} M_{\rm ap}^i}{M_m^i - M_m^{i+1} - M_{\rm ap}^i + M_{\rm ap}^{i+1}}. \tag{13}$$

Once the true mass is determined, we use equations (10) and (12) to determine the S/N of the peak:

$$S/N = \sqrt{M/\mathcal{C}(M)}. \tag{14}$$

Given our two selection criteria, in the above example the point of local maximum will be selected as a peak by the filter $i + 1$, but not by its predecessor i, if the S/N will also be above the detection threshold. It will also appear as a peak in the maps smoothed with filters $< M_m^{i+1}$, provided that the same S/N requirement is fulfilled. In order to be able to carry out the interpolation scheme, for each filter used we record the aperture mass, S/N and the 2D location of the peaks. A peak might slightly change its coordinates in maps smoothed with different-sized filters; we take this into account, and allow for variations of up to 4 pixels in the $\hat{\mathbf{x}}$, $\hat{\mathbf{y}}$ directions of the map (a pixel has $\theta_{\rm pix} = 10$ arcsec). We also record those points of maximum where the aperture mass is smaller, but not much smaller than the mass of the respective filter; to be specific, the points obeying the condition: $0.6 M_m^i < M_{\rm ap}^i < M_m^i$. These points

we call 'pseudo-peaks' and they are likely to be selected as peaks by the next filter in the sequence; therefore, they are useful for the interpolation that we perform later. The value 0.6 is of no particular significance, it is suitable for the logarithmically spaced sequence of filters that we apply, based on several trials.

Finally, the processing of the peaks resulting from the smoothing with the hierarchical sequence of filters, consists of the following steps. (1) We exclude from the maps those peaks already selected by a larger filter. (2) We apply the interpolation scheme to assign the remaining peaks a unique aperture mass, according to equation (13). We then use this mass to compute the S/N value, according to equation (14). (3) We exclude those peaks that are within the virial radius of a larger peak, since in many of such cases, the second peak is just an artefact of the smoothing or we simply deal with a very clumpy halo that is split by the smoothing into a large peak and some small ones. We thus remove the problem of 'peaks-in-peaks' and also do not count substructures as independent haloes. This is done for the purpose of obtaining a 'clean' peak function, but ultimately such events concern only small peaks and we have checked that the cosmological constraints derived from the counts are not significantly altered by these exclusions.

3.3 Model specifications

We base our halo model on the NFW density profile:

$$\rho_{\mathrm{NFW}}(r) = \bar{\rho}\,\delta_{\mathrm{c}}\left[\frac{r}{r_{\mathrm{s}}}\left(1+\frac{r}{r_{\mathrm{s}}}\right)^2\right]^{-1}, \tag{15}$$

where $\bar{\rho}$ is the mean matter density of the Universe, δ_{c} is the characteristic overdensity and r_{s} is the scale radius. We adopt the Sheth–Tormen (ST) definition of mass (Sheth & Tormen 1999): $M_{\mathrm{vir}} = 4\pi R_{\mathrm{vir}}^3 \Delta_{\mathrm{vir}} \bar{\rho}/3$, i.e. we use the mean matter density to define the overdensity for halo formation, as opposed to the critical density, ρ_{crit}. The two are related by $\bar{\rho} = \Omega_{\mathrm{m}}\rho_{\mathrm{crit}}$. $\Delta_{\mathrm{vir}} = 200$ for ST and NFW. Integrating equation (15) to obtain the virial mass and using the above definition for the latter, one arrives at the following expression for the characteristic overdensity:

$$\delta_{\mathrm{c}} = \frac{\Delta_{\mathrm{vir}}\,c^3/3}{\log(1+c) - c/(1+c)}, \tag{16}$$

where the concentration parameter is defined by $c = R_{\mathrm{vir}}/r_{\mathrm{s}}$. In the Λ cold dark matter (ΛCDM) model, ST and NFW haloes have the same density profile, but ST haloes have larger cut-off radii and concentration parameters than NFW ones. For the concentration parameter we employed the numerical prescription of Gao et al. (2008), whilst to translate NFW to ST parameters, we used the approach of Smith & Watts (2005).

We use the truncated convergence profile resulting from this profile, i.e. we limit the projection of the 3D density along the line of sight to a region delimited by the virial radius:

$$\kappa_{\mathrm{NFW}}(r_\perp) = \frac{1}{\Sigma_{\mathrm{crit}}}\int_{-\sqrt{R_{\mathrm{vir}}^2-r_\perp^2}}^{\sqrt{R_{\mathrm{vir}}^2-r_\perp^2}} \mathrm{d}z\,\rho_{\mathrm{NFW}}(\sqrt{r_\perp^2+z^2}), \tag{17}$$

with Σ_{crit} being the critical surface density for lensing. The above equation can be rewritten as

$$\kappa_{\mathrm{NFW}}(x) = \frac{2\,r_{\mathrm{s}}\,\delta_{\mathrm{c}}\,\bar{\rho}}{\Sigma_{\mathrm{crit}}}\,f(x), \tag{18}$$

where $x = r_\perp/r_{\mathrm{s}}$ is adimensional, and the function f depends on cosmology only through the concentration parameter (Hamana et al. 2004):

$$f(x) = \begin{cases} -\dfrac{(c^2-x^2)^{1/2}}{(1-x^2)(1+c)} + \dfrac{\cosh^{-1}\left(\frac{x^2+c}{x(1+c)}\right)}{(1-x^2)^{3/2}}, & x<1, \\[4mm] \dfrac{(c^2-1)^{1/2}}{3(1+c)}\left(1+\dfrac{1}{1+c}\right), & x=1, \\[4mm] -\dfrac{(c^2-x^2)^{1/2}}{(1-x^2)(1+c)} - \dfrac{\cos^{-1}\left(\frac{x^2+c}{x(1+c)}\right)}{(x^2-1)^{3/2}}, & x>1, \\[4mm] 0, & x>c. \end{cases} \tag{19}$$

The model that we assume for the κ of haloes is a convolution of the NFW convergence profile defined by equation (19) with a two-dimensional (2D) Gaussian function with the width of the order of the softening length of the simulations:

$$\kappa_{\mathrm{m}}(\boldsymbol{\theta}) = \int \mathrm{d}^2\theta'\,\kappa_{\mathrm{NFW}}(\boldsymbol{\theta}')\,G_{\mathrm{2D}}(\boldsymbol{\theta}-\boldsymbol{\theta}'). \tag{20}$$

The above equation can be rewritten as

$$\kappa_{\mathrm{m}}(\boldsymbol{\theta}) = \frac{\exp\left(\frac{-\theta^2}{2\sigma_{\mathrm{G}}^2}\right)}{\sigma_{\mathrm{G}}^2}$$
$$\times \int_0^\infty \mathrm{d}\theta'\,\theta'\kappa_{\mathrm{NFW}}(\theta')\exp\left(\frac{-\theta'^2}{2\sigma_{\mathrm{G}}^2}\right)I_0\left(\frac{-\theta\,\theta'}{\sigma_{\mathrm{G}}^2}\right), \tag{21}$$

where σ_{G} is the width of the Gaussian function, and I_0 is the modified Bessel function of order 0. The dependence on the lens redshift is implicit for both κ_{NFW} and σ_{G}. This model choice accounts for the finite resolution of the numerical simulations. The convolution in equation (21) has a similar effect to 'coring' the convergence profile, i.e. making it flat in the centre of the cluster, where the WL regime breaks down and measurements are very difficult to obtain. For numerical simulations, cored profile models are desirable because one cannot resolve structures below the softening length. Lastly, equation (21) alleviates uncertainties in the location of the centre of the peak, which could lead to large discrepancies between measured and theoretical profiles, if the latter have a cusp at the centre, e.g. like NFW. Therefore, we take the width of the Gaussian present in the convolution to be $\sigma_{\mathrm{G}} = \alpha\,l_{\mathrm{soft}}$, where l_{soft} is the softening length of the simulations, $\alpha = 2$ for ST haloes with $M \geq 7 \times 10^{14}\,h^{-1}\,\mathrm{M}_\odot$, and $\alpha = 1.5$ for $M < 7 \times 10^{14}\,h^{-1}\,\mathrm{M}_\odot$. For the redshift $z_{\mathrm{m}} = 0.3$ that we assume for our filter, $\sigma_{\mathrm{G}} = 22\,(29)$ arcsec, respectively.

Fig. 2 shows the comparison of the theoretical and measured profiles for the unfiltered convergence maps of the fiducial model corresponding to sources at redshift 1, in the absence of shape noise. We use the hierarchical method to assign masses to peaks. The peaks are binned according to the assigned mass, and the coordinates of their centres are used to measure the shear and convergence profiles. Each panel in the figure corresponds to a mass bin. The red points depict the average of the measured convergence profiles of the detected peaks. The error bars correspond to errors on the mean of the 128 fiducial fields. The solid blue lines represent the theoretical profile of equation (21), estimated for the mean mass of the peaks in the bin and the redshift $z_{\mathrm{m}} = 0.3$, i.e. the optimal redshift for lensing for sources at redshift 1. The agreement between the model and measurements is remarkable, given the fact that some peaks correspond to haloes at different redshifts or to no haloes at all, and the fact that we assume a spherical density model, which is bound to fail for peaks arising from aspherical haloes, or to be affected by projection effects. Despite these limitations, the hierarchical method
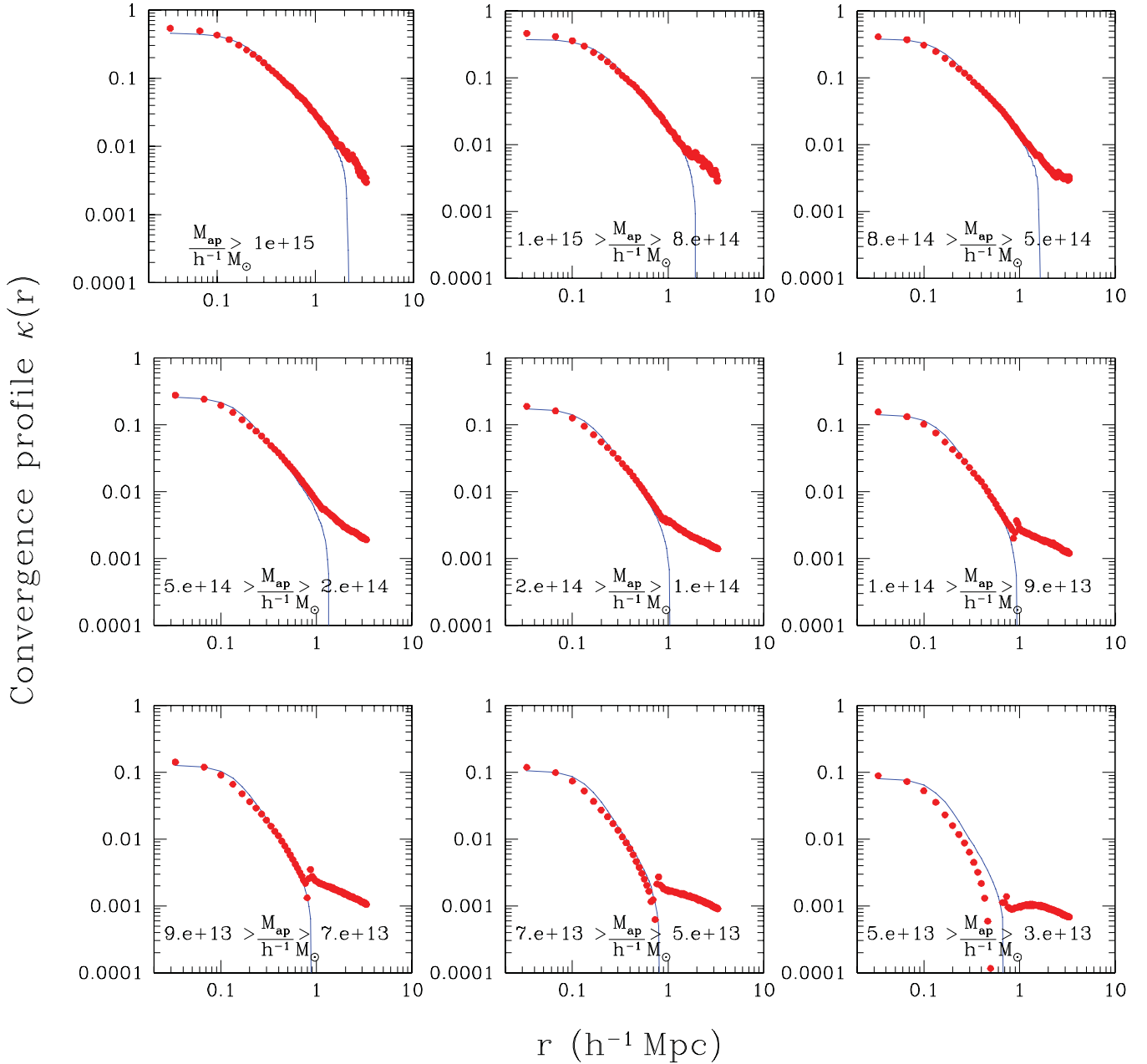
Figure 2. Comparison between measured and theoretical convergence profiles for the unsmoothed fiducial cosmology maps, with the sources at redshift 1. The red points represent the average of the measured profiles around the centres of the peaks detected with the hierarchical method of Section 3.2. The peaks have been binned according to the mass assigned through that method, and the panels depict different mass bins. The blue solid lines represent the theoretical profile from equation (21), for the mean mass of the bin. The redshift of the filter is set at 0.3, and the error bars are on the mean of 128 fields. The maps are free of shape noise.

classifies peaks efficiently on average, as shown in the figure. Note that the bottom panels of Fig. 2 present an oscillatory feature around the virial radius of the profiles. We generated convergence maps of synthetic, perfect NFW haloes, and checked that such features can appear if noise is added to the maps. This owes to the fact that the compensated filter prefers to select peaks which have regions of low convergence around the virial radius. This effect is more pronounced for smaller peaks because these most likely correspond to small haloes, which have increased particle shot noise. We have measured the convergence profiles of the friends-of-friends (FoF) haloes of the simulations at redshift 0.3, and did not find such

features as seen in Fig. 2, from which we conclude that they are caused by the filter selection.

We use the above-mentioned values for α in equation (21) to obtain Fig. 2; based on several trials, we find these values to yield the closest resemblance between the measured and theoretical profiles. We do this test in the absence of shape noise, since we are trying to address a technical issue arising from our numerical simulations: the impact of the softening length. In the absence of shape noise, the algorithm in Section 3.2 can be applied by formally setting $\sigma_\gamma^2/\bar{n} \rightarrow 1$ in equation (4), and using only the mass criterion to select peaks; equation (10) does not change.

The hierarchical method could be useful for determining cluster masses from WL profiles. In order to increase the accuracy of the results, one should perform a careful analysis of the chosen filter and its parameters, the compensation radius θ_A, the inclusion of the halo-matter cross-correlation term visible in Fig. 2, the impact of shape noise and projection noise and the impact of photometric redshifts errors of the source galaxies. However, this is beyond the goals of the present study.

4 RESULTS

We present a comparison between peak statistics results obtained through the hierarchical algorithm described in Section 3 and from applying three single-sized filters of different size. When using the single-sized filters, we keep the same filter function as given in Section 3, as this work is not concerned with assessing the performance of filters of different shape. In this case, we simply select the peaks by requiring that their $S/N \geq (S/N)_{min}$, with the S/N given by equation (6). The three sizes that we consider correspond at redshift $z_m = 0.3$ to the masses $\{2 \times 10^{15}, 5.5 \times 10^{14}, 10^{14}\}\, h^{-1}\, M_\odot$, with the angular size of the virial radii given by $\{13.2, 8.6, 4.8\}$ arcmin, respectively. Note that due to the fact that ST haloes have larger radii than NFW ones of the same mass, these angular sizes are also slightly larger than NFW angular sizes. For the hierarchical filter we consider a series of 12 filters, logarithmically spanning the mass interval $[8.85 \times 10^{13}, 2 \times 10^{15}]\, h^{-1}\, M_\odot$, and with $S/N \geq 2.6$. Ultimately, throughout the entire analysis for the fixed size and hierarchical methods, we shall use only peaks above the threshold $(S/N)_{min} = 2.8$, but going to lower values ensures the completeness of the sample of hierarchical peaks. The shape noise contamination makes it difficult to consider smaller filters. We bin the resulting peak abundances in terms of S/N, logarithmically spanning an interval $[2.8, 14]$. For reasons discussed in Appendix B, we choose $N_{bin} = 20$. Note that for the hierarchical abundance it is useful to also consider binning in mass, as assigned through equations (10), (12) and (13). This allows us to draw analogies between the properties of the WL peaks and those of 3D haloes. Here too we use 20 bins spanning $[10^{14}, 2 \times 10^{15}]\, h^{-1}\, M_\odot$, the lower bound roughly corresponding to the $(S/N)_{min} = 2.8$ for the analysed cosmological models.

Comparing peak abundances obtained with different methods is not necessarily relevant: the results will be clearly different, and it would be hard to decide which filter size is more effective. This is shown in Fig. 3, where we present the peak functions corresponding to the three single-sized filters, as well as the hierarchical method. The functions are expressed as number of peaks per unit S/N for an area of $144\, \mathrm{deg}^2$, and the results are an average of the peak functions measured in the 128 fields of the fiducial model. The error bars correspond to errors on the mean. As expected, each single-sized filter favours the detection of peaks with S/N in accord to its size: the smallest filter peak abundance is mostly formed by low S/N peaks, and similarly for the medium and large filters. The hierarchical peak abundance is similar to the largest filter abundance for the high-S/N bins, and to the smallest filter abundance for the low-S/N bins. We shall next explore how the measured abundances translate into cosmological constraints.

To this effect, we shall resort to the Fisher matrix formalism, with four clear goals:

(i) to provide a comparison between the filtering methods;
(ii) to test which range of mass or S/N contributes most to the constraints derived from WL peak counts;
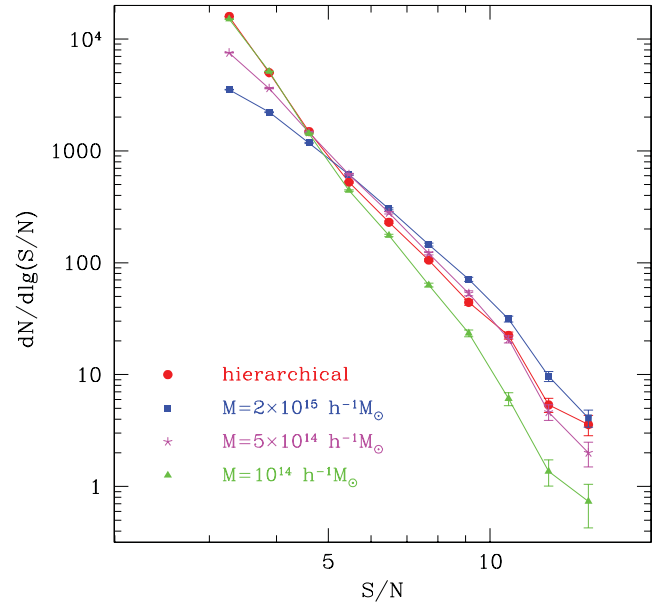

Figure 3. The number of peaks per unit S/N for an area of $144\, \mathrm{deg}^2$. Different symbols and colours denote different filter sizes: red circles correspond to the hierarchical filtering, and blue squares/purple stars/green triangles to the $M = 2 \times 10^{15}, 5 \times 10^{14}, 10^{14}\, h^{-1}\, M_\odot$ filters, respectively. The redshift of the filter is kept fixed throughout the analysis at $z_m = 0.3$. The results are the mean of the functions measured from 128 fields of the fiducial cosmology, and the error bars are on the mean.

(iii) to test the difference between the errors obtained by using the full covariance matrix of counts, and the Poisson errors;

(iv) to provide a realistic forecast for surveys like LSST and *Euclid*, in a very direct manner, based on simulation measurements.

4.1 Fisher matrix considerations

Using the measured peak abundances, we compute the Fisher information following the standard definition:

$$\mathcal{F}_{p_a p_b} = -\left\langle \frac{\partial^2 \ln \mathcal{L}}{\partial p_a \partial p_b} \right\rangle, \tag{22}$$

where p_a and p_b are elements of the cosmological model parameter set $\boldsymbol{p}$ upon which the likelihood $\mathcal{L}$ depends. In our case the set is $\{n, \sigma_8, \Omega_m, w\}$. We assume a Gaussian likelihood

$$\mathcal{L}(\boldsymbol{m} \,|\, \bar{\boldsymbol{m}}(\boldsymbol{p}), \mathbf{C}(\boldsymbol{p})) = \frac{1}{(2\pi)^{N_{bin}/2} |\mathbf{C}|^{1/2}}$$
$$\times \exp\left[-\frac{1}{2}(\boldsymbol{m} - \bar{\boldsymbol{m}})^{\mathrm{t}} \mathbf{C}^{-1}(\boldsymbol{m} - \bar{\boldsymbol{m}}) \right], \tag{23}$$

where $\boldsymbol{m}$ is the vector of peak counts, and $\bar{\boldsymbol{m}}$ is the vector of mean number of peaks; both vectors have the dimension N_{bin}, i.e. the number of bins considered. The covariance matrix of the counts in bins i and j is

$$C_{ij} = \langle (m_i - \bar{m}_i)(m_j - \bar{m}_j) \rangle. \tag{24}$$

From the Fisher matrix, one may obtain an estimate of the marginalized errors and covariances of the parameters:

$$\sigma^2_{p_a p_b} = [\mathcal{F}^{-1}]_{p_a p_b}, \tag{25}$$

as well as the unmarginalized errors:

$$\sigma_{p_a} = [\mathcal{F}_{p_a p_a}]^{-1/2}. \tag{26}$$

The size of the errors quantifies the efficiency of the filtering method to extract cosmological information from WL peak counts. For simplicity, we shall ignore the trace term in the Fisher matrix, (Tegmark, Taylor & Heavens 1997). In this case, equation (22) can be rewritten as

$$\mathcal{F}_{p_a\,p_b} = \sum_{i,j} \frac{\partial \bar{m}_i}{\partial p_a} C_{ij}^{-1} \frac{\partial \bar{m}_j}{\partial p_b}. \tag{27}$$

We are also interested in the Poisson errors of the peak counts, since the Poisson statistic is widely adopted in forecasting cosmological constraints from WL peak counts. They are given by

$$\mathcal{F}_{p_a\,p_b}^{P} = \sum_{i} \frac{\partial \bar{m}_i}{\partial p_a} \frac{\partial \bar{m}_i}{\partial p_b} \frac{1}{\bar{m}_i}. \tag{28}$$

The mean number of counts for bin i is estimated as

$$\hat{\bar{m}}_i = \frac{1}{N} \sum_{f=1}^{N} m_i^f. \tag{29}$$

In the above f designates the field number, while N is the total number of fields; for the fiducial cosmology, $N = 128$, and for the variational cosmologies, $N = 64$. An unbiased, maximum-likelihood estimator for the covariance matrix is

$$\hat{C}_{ij} = \frac{1}{N-1} \sum_{f=1}^{N} \left(m_i^f - \hat{\bar{m}}_i \right) \left(m_j^f - \hat{\bar{m}}_j \right). \tag{30}$$

The derivatives of the counts with respect to the cosmological parameters are calculated from

$$\widehat{\frac{\partial \bar{m}_i}{\partial p_a}} = \frac{1}{N} \sum_{f=1}^{N} \frac{m_i^f(p_a + \Delta p_a) - m_i^f(p_a - \Delta p_a)}{2\Delta p_a}, \tag{31}$$

where Δp_a represents the $\pm$ step in the cosmological parameters, e.g. Table 1.

We estimate the Fisher matrix errors using the covariance on the mean for the counts of the fiducial model; the rescaled covariance matrix corresponds to an area of $\approx 18\,000\ \deg^2$. Together with the survey specifications given in Section 2, this makes our study representative for two future surveys, LSST and *Euclid*.

4.2 Comparison of filtering methods

Fig. 4 depicts the derivatives of the measured peak abundances with respect to the four cosmological parameters that we consider, as a function of S/N. We show results for the hierarchical method and the largest of the single-sized filters, $M = 2 \times 10^{15}\,h^{-1}\,\mathrm{M}_\odot$. The derivatives are estimated using equation (31), and the result is divided by the mean counts of the fiducial cosmology. The figure shows that both filtering methods yield peak functions similarly sensitive to cosmology, with the hierarchical derivatives displaying slightly more features than the single-sized ones. For most of the S/N range considered, the peak-function derivatives are non-zero, signifying that there is cosmological information in the high-S/N peaks, as well as in the low-S/N ones, as previously noticed by Dietrich & Hartlap (2010). This originates in a similar behaviour displayed by the halo mass function: in a previous work (Smith & Marian 2011), we found the derivatives of the latter with respect to the same parameters studied here to be non-zero for a large range of halo masses, down to $M = 10^{13}\,h^{-1}\,\mathrm{M}_\odot$ (compare figs 6 and 7 in that work with Figs 4 and 5 in this work).

Fig. 5 depicts the marginalized Fisher errors for the four cosmological parameters that we consider. The errors are fractional, i.e. the error for each parameter is divided by the fiducial value of that
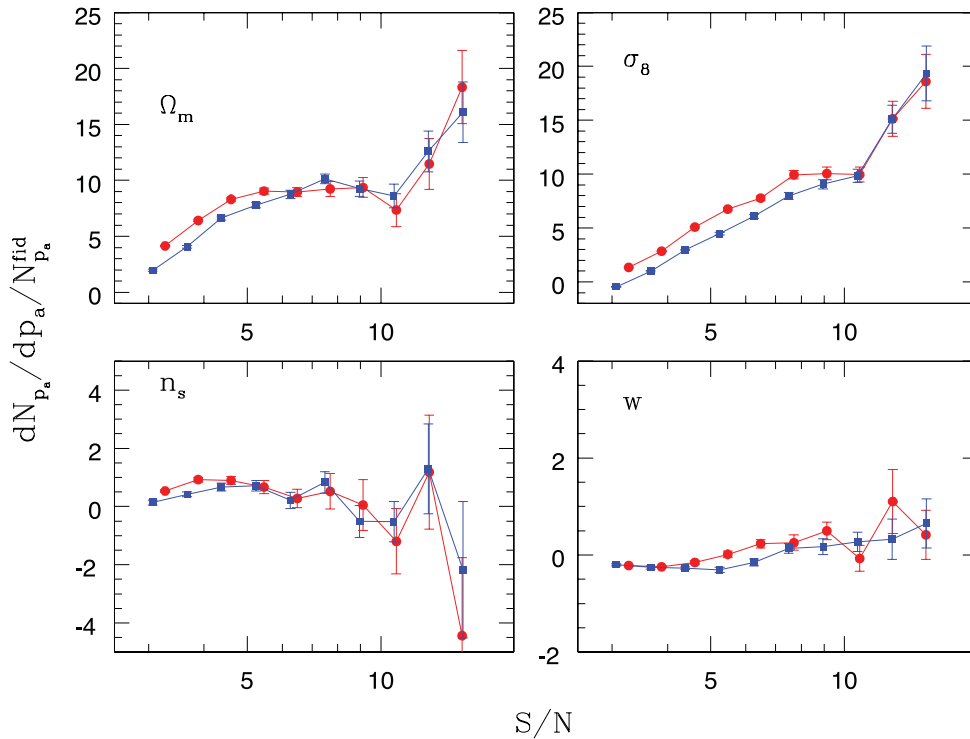

Figure 4. Derivatives of the peak abundances with respect to the cosmological parameters considered, as a function of S/N. The red solid circles are measurements with the hierarchical method, and the blue solid squares correspond to smoothing with a filter of fixed size $M = 2 \times 10^{15}\,h^{-1}\,\mathrm{M}_\odot$ (angular size of the radius 13.2 arcmin for $z_m = 0.3$). The derivatives are estimated in accord with equation (31), and are divided by the mean counts of the fiducial model. We show the errors on the mean of 64 fields.
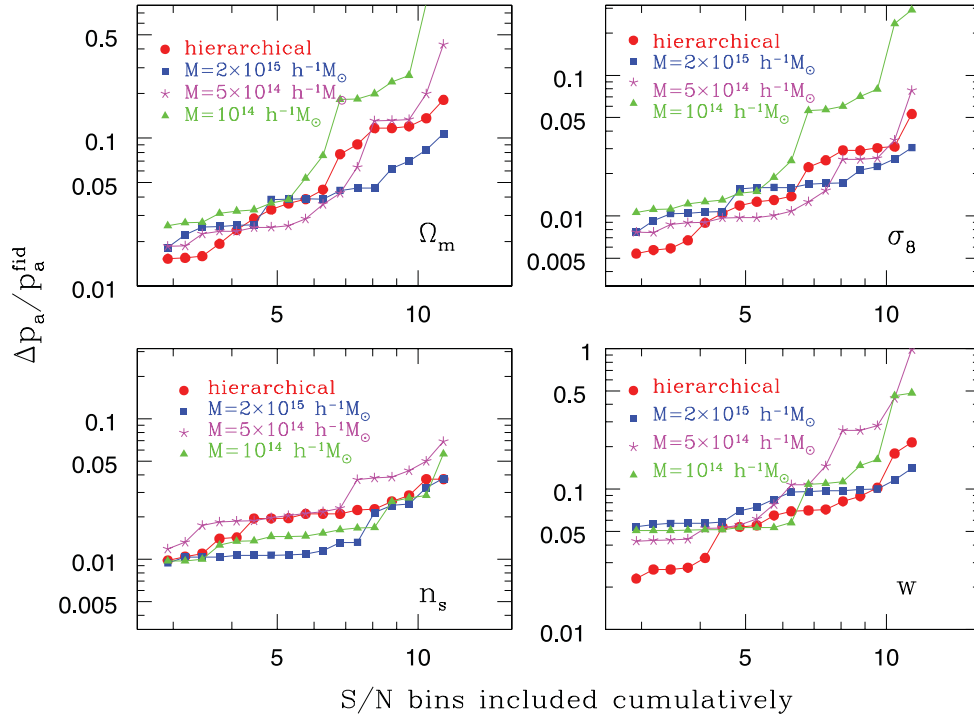
Figure 5. Fractional marginalized Fisher matrix errors based on measurements from simulations. The symbols and colours are the same as in Fig. 3. The errors are cumulative: starting from the highest bins, we gradually allow the rest of the bins to contribute to the constraints. The central values of the S/N bins are indicated on the $\hat{\mathbf{x}}$-axis.

parameter, and cumulative, i.e. we include S/N bins cumulatively, from the largest to the lowest. The central values of the bins are indicated on the $\hat{\mathbf{x}}$-axis. The symbols and colours are the same as in Fig. 3. It is apparent that the hierarchical filtering performs better than the single-sized filtering, if one takes into account peaks with S/N ≤ 4. The greatest improvement is for w: the hierarchical error is smaller by more than a factor of 2 compared to the fixed-size filtering. A smaller improvement happens also in the case of σ_8 and Ω_m, while the error on n_s seems unaffected by the filtering method, due to generally poor constraining power that peaks have on this parameter. Fig. 5 reinforces the suggestion of Fig. 4 that the inclusion of peaks with small S/N improves significantly the cosmological information.

Note that for the hierarchical method we can also use aperture-mass bins to measure the peak function derivatives, the covariance matrix and the Fisher matrix, with the mass given by equation (13). We obtain similar results to those presented in Figs 4 and 5. The single-sized filters perform very similarly, the largest one being marginally better in the case of Ω_m, σ_8 and n_s. Its diameter of 13.2 arcmin is larger than what previous studies in the literature have used: Hamana et al. (2004) had a 1-arcmin Gaussian filter, Hennawi & Spergel (2005) employed a $\sim$5-arcmin NFW filter and Dietrich & Hartlap (2010) a 5.6-arcmin one. Since the constraints from filtering with fixed sizes are so similar, we shall only show the results from the marginally better $M = 2 \times 10^{15}\,h^{-1}\,\mathrm{M}_\odot$ one.

In Appendix A we examine the statistical properties of the peaks detected through the hierarchical and fixed-sized methods. We find the following.

(i) The Poisson statistic describes well the distribution of hierarchical high-S/N and high-mass peaks. The mass is defined by equation (13). We show that the correlation matrix of S/N-binned hierarchical peaks has strong off-diagonal contributions for

the small-S/N bins, while being largely diagonal for the large-S/N bins. The same applies to the mass-binned correlation coefficient, and this behaviour is similar to that of haloes, as shown in Smith & Marian (2011).

(ii) The high-S/N single-sized peaks are also reasonably described by the Poisson distribution, due to the fact that such peaks are usually quite massive and rare. The correlation matrix of these peaks seems slightly more correlated for S/N ≥ 7 than the hierarchical matrix.

Lastly, in Appendix B we investigate the dependence of the Fisher errors on the number of bins in which the S/N interval is divided. Fig. B1 suggests that all filtering methods reach the expected saturation in information if $N_{bin} \leq 20$, which is why we choose $N_{bin} = 20$ for the results presented in this work.

4.3 Forecasting constraints on cosmology

We present a Fisher-matrix forecast for the four-dimensional cosmological parameter space explored in this work. This will enable us to compare the filtering methods in a more realistic context, using marginalized errors and also cosmic microwave background (CMB) information.

For the *Planck* Fisher matrix, we shall assume that the CMB temperature and polarization spectra can constrain nine parameters: the dark energy equation-of-state parameters w_0 and w_a; the density parameter for dark energy Ω_{DE}; the CDM and baryon density parameters scaled by the square of the dimensionless Hubble parameter $\omega_{CDM} = \Omega_{CDM}h^2$ and $\omega_b = \Omega_b h^2$ ($h = H_0/[100\,\mathrm{km\,s^{-1}\,Mpc^{-1}}]$); the primordial spectral index of scalar perturbations n_s; the primordial amplitude of scalar perturbations A_s; the running of the spectral index α and the optical depth to the last scattering surface τ. To compute the CMB Fisher matrix we follow Eisenstein,

Table 3. Fisher matrix constraints for the hierarchical method and a fixed filter of $M = 2 \times 10^{15}\, h^{-1}\, \mathrm{M}_\odot$. The fiducial values for the parameters are $n_s = 1$, $\Omega_m = 0.25$, $\sigma_8 = 0.8$ and $w = -1$.

| | Hierarchical errors | | | | Fixed-size errors | | | |
	n_s	Ω_m	σ_8	w	n_s	Ω_m	σ_8	w
Unmarginalized	0.0025	0.0006	0.0015	0.0125	0.0064	0.0008	0.0019	0.0128
Marginalized	0.0094	0.0038	0.0043	0.0235	0.0105	0.0046	0.0061	0.0552
Marginalized + CMB	0.0039	0.002	0.003	0.019	0.004	0.0045	0.006	0.0525

Hu & Tegmark (1999):

$$\mathcal{F}_{p_a p_b} = \sum_l \sum_{X,Y} \frac{\partial C_{l,X}}{\partial p_a} \mathrm{Cov}^{-1}\left[C_{l,X}, C_{l,Y}\right] \frac{\partial C_{l,Y}}{\partial p_b}, \tag{32}$$

where $\{X, Y\} \in \{\mathrm{TT}, \mathrm{EE}, \mathrm{TE}, \mathrm{BB}\}$, where $C_{l,\mathrm{TT}}$ is the temperature power spectrum, $C_{l,\mathrm{EE}}$ is the E-mode polarization power spectrum, $C_{l,\mathrm{TE}}$ is the temperature–E-mode polarization cross-power spectrum and $C_{l,\mathrm{BB}}$ is the B-mode polarization power spectrum. The assumed sky coverage is $f_{\mathrm{sky}} = 0.8$. In order to make the CMB Fisher matrix compatible with our parameters, we rotate it to a new set

$$\mathbf{q}^\mathrm{T} = \{w_0, w_a, \Omega_m, h, f_b, \tau, n_s, \sigma_8, \alpha\}, \tag{33}$$

where for us $w_0 = w$. We marginalize over the five parameters absent from our analysis.

Table 3 and Fig. 6 represent the main results of this work, showing the overall improvement the hierarchical method brings over the fixed-size method after marginalization and especially after the

inclusion of the CMB information. For the fixed-size method we choose the filter with $M = 2 \times 10^{15}\, h^{-1}\, \mathrm{M}_\odot$, i.e. the best-performing filter among the fixed sizes that we have probed. We also show the unmarginalized errors, for a more complete picture.

Combined with the CMB, the hierarchical errors are a factor of 2 better than the single-filter method for Ω_m and σ_8, and almost a factor of 3 better for w. For n_s there is no significant difference between the filtering methods. This happens because the CMB constrains the primordial power spectrum tighter than WL peak counts.

We further depict these results in Fig. 6 as 2σ ellipses; the blue dashed ellipses correspond to the single-sized method, and the red solid ones to the hierarchical algorithm. Here we see again that the latter really improves the joint constraints for $\{\sigma_8, \Omega_m, w\}$.

It is difficult to make a comparison to previous forecasts in the literature, as the probed parameter space and survey specifications are not the same, so we shall mention only two. Wang et al. (2004) presented a forecast for LSST in which besides WL counts
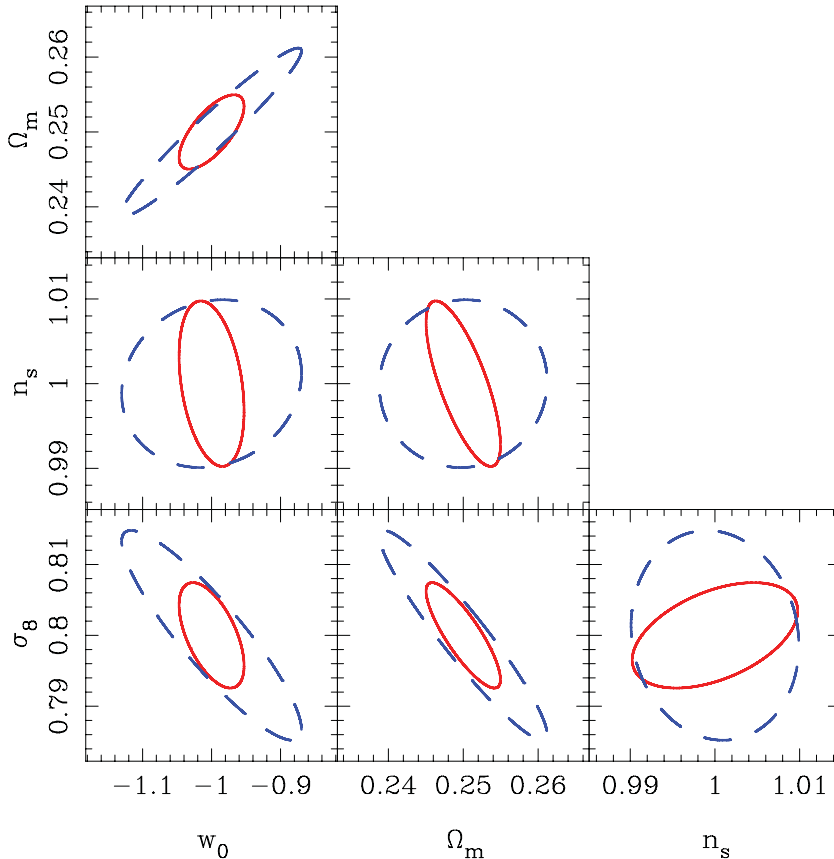

Figure 6. Forecasted marginalized errors for WL peak counts from a *Euclid* type of survey combined with CMB constraints from *Planck*. The blue dashed ellipses depict the results of the fixed filter $M = 2 \times 10^{15}\, h^{-1}\, \mathrm{M}_\odot$, while the red solid ellipses correspond to the hierarchical method. In both cases, the WL Fisher matrix has been added to the *Planck* Fisher matrix, and the constraints are at the 2σ level.

they also include the cluster power spectrum, which they treat as completely independent. They consider a larger parameter space than ours, including w_a and ω_b, and assume $\bar{n} = 65$ arcmin^{-2} and $(S/N)_{min} = 4.5$. The constraints that they find when combined with *Planck* priors (see table 6 in their paper) are $\Delta n_s = 0.0022$, $\Delta\Omega_{DE} = 0.0033$, $\Delta\sigma_8 = 0.0037$ and $\Delta w = 0.036$. They use a Gaussian filter of size 1 arcmin, and their fiducial model has $\Omega_m = 0.27$, $\sigma_8 = 0.9$. The results are rather similar to ours, though their constraint of w is surprisingly tight, given the sensitivity of Δw to $(S/N)_{min}$ – higher than ours – and the fact that they include w_a, known to degrade substantially the constraint on w.

We also make a comparison to our previous work (Marian & Bernstein 2006), which uses the same type of normalized filter as this study. The detection threshold is 5, the projection noise is accounted for, and instead of n_s, w_a is considered. The fiducial values for Ω_m and σ_8 are the same as in Wang et al. (2004); combining with the *Planck* information, we found the constraints: $\Delta\Omega_m = 0.005$, $\Delta\sigma_8 = 0.004$, $\Delta w = 0.063$. These are in agreement with the results from the present study, given the above-mentioned differences.

5 SUMMARY AND CONCLUSIONS

In this paper we proposed a new method, which we called 'the hierarchical algorithm' to detect and explore WL peak counts. While previous studies have examined the benefits of using filters of a certain shape (Hennawi & Spergel 2005; Maturi et al. 2005; Gruen et al. 2011), here we have focused on the way the filtering should be performed to maximize the inferred cosmological constraints. To this goal, we have used a large set of WL maps produced by ray tracing through *N*-body simulations with varying cosmological models, as described in Section 2.

Our method was based on the idea of sequential smoothing of the maps with filters of different size, from the largest to the smallest. The chosen filter was an aperture-mass filter, matching the NFW density profile of haloes. Combining the information contained in the maps smoothed on different scales, we determined the largest filter size for which a peak would not only be a point of local maximum, with a S/N larger than a certain threshold, but also a match to the NFW profile of the filter. For the latter we have assumed a fixed redshift equal to the optimal redshift for lensing given the mean redshift of the source distribution. Under this assumption, we assigned a unique value of mass and S/N to the detected peaks, as described in detail in Section 3. Thus, the peak function arising from the hierarchical method does not depend on a particular filter size.

We compared the hierarchical peak abundance to that obtained from applying a filter of fixed size; for the latter we used the same aperture filter and considered three sizes $\{13.2, 8.6, 4.8\}$ arcmin. At the assumed redshift $z_m = 0.3$, these correspond to haloes with a Sheth–Tormen mass of $M = \{2 \times 10^{15}, 5 \times 10^{14}, 10^{14}\}\, h^{-1}\,M_\odot$. To quantify the efficiency of the smoothing methods, we took the Fisher matrix approach: we compared the errors on the cosmological parameters derived from each method. The considered parameters were $\{n_s, \Omega_m, \sigma_8, w\}$. Our findings are as follows.

(i) The marginalized Fisher matrix errors obtained from the hierarchical peak abundance combined with CMB information from *Planck* were better by a factor of ≈ 2 compared to the results of the single-sized filtering. This was true if we took into account low peaks with S/N ~ 3; if we allowed only peaks with S/N ≥ 6, then the hierarchical errors were only marginally better.

(ii) The three filters of fixed size yield very similar results, the largest being slightly more effective.

(iii) We have provided a cosmology forecast for WL peak counts relevant to future surveys like *Euclid* and LSST. Combined with information from a CMB experiment such as *Planck*, the hierarchical marginalized errors for the considered parameters were $\Delta n_s = 0.0039\,(0.004)$, $\Delta\Omega_m = 0.002\,(0.0045)$, $\Delta\sigma_8 = 0.003\,(0.006)$ and $\Delta w = 0.019\,(0.0525)$, where the values in the parenthesis corresponded to the results of the largest, fixed-size filter. Note that we have assumed no knowledge of the redshifts of the peaks, and yet have obtained values in a reasonable accord with analytical forecasts in the literature.

(iv) The high-S/N and high-mass ends of the hierarchical peak function were reasonably described by the Poisson distribution, e.g. Figs A1, A2, A5 and A6, since the hierarchical filtering successfully assigned the largest mass and S/N to the largest and rarest peaks.

(v) The results of the Fisher matrix analysis had a slight dependence on the number of S/N bins used: the most suitable number of bins for the hierarchical method was 20.

We have checked that the hierarchical method yields similar constraints if one bins the peak information in mass and not S/N, which is a reassuring consistency check.

There are certain improvements that one could bring to the hierarchical method. First, the choice of filter shape: in this study, we have resorted to a filter which is optimal if one assumes the shape noise of galaxies as the main source of noise for WL measurements. Though this filter is also effective in reducing the impact of correlated line-of-sight projections for the measured peaks (Marian et al. 2009, 2010), one could use a more sophisticated shape, as discussed in Gruen et al. (2011). Secondly, one should test the benefits of having more redshift information on the source galaxies, i.e. use tomography to improve the cosmological constraints derived from the peak abundance. We defer these issues to a future study.

The main message conveyed by our work is that, compared to the standard approach of single-sized smoothing usually discussed in the literature, the hierarchical method extracts significantly more of the cosmological information enclosed in WL peak counts. Therefore, it will be a very useful tool for surveys like *Euclid* and LSST which have the potential to detect many thousands of peaks.

REFERENCES

Abate A., Wittman D., Margoniner V. E., Bridle S. L., Gee P., Tyson J. A., Dell'Antonio I. P., 2009, ApJ, 702, 603
Albrecht A. et al., 2006, ArXiv e-prints

Becker M. R., Kravtsov A. V., 2011, ApJ, 740, 25

Bergé J. et al., 2008, MNRAS, 385, 695

Clowe D., De Lucia G., King L., 2004, MNRAS, 350, 1038

Crocce M., Pueblas S., Scoccimarro R., 2006, MNRAS, 373, 369

Dahle H., 2006, ApJ, 653, 954

Dietrich J. P., Hartlap J., 2010, MNRAS, 402, 1049

Eisenstein D. J., Hu W., Tegmark M., 1999, ApJ, 518, 2

Gao L., Navarro J. F., Cole S., Frenk C. S., White S. D. M., Springel V., Jenkins A., Neto A. F., 2008, MNRAS, 387, 536

Gruen D., Bernstein G. M., Lam T. Y., Seitz S., 2011, MNRAS, 416, 1392

Hamana T., Takada M., Yoshida N., 2004, MNRAS, 350, 893

Hartlap J., Simon P., Schneider P., 2007, A&A, 464, 399

Hennawi J. F., Spergel D. N., 2005, ApJ, 624, 59

Hetterscheidt M., Simon P., Schirmer M., Hildebrandt H., Schrabback T., Erben T., Schneider P., 2007, A&A, 468, 859

Hilbert S., White S. D. M., Hartlap J., Schneider P., 2007a, MNRAS, 382, 121

Hilbert S., Metcalf R. B., White S. D. M., 2007b, MNRAS, 382, 1494

Hilbert S., Hartlap J., White S. D. M., Schneider P., 2009, A&A, 499, 31

Hoekstra H., 2001, A&A, 370, 743

Hoekstra H. et al., 2006, ApJ, 647, 116

Israel H. et al., 2010, A&A, 520, A58

Jarvis M., Bernstein G. M., Fischer P., Smith D., Jain B., Tyson J. A., Wittman D., 2003, AJ, 125, 1014

Jarvis M., Jain B., Bernstein G., Dolney D., 2006, ApJ, 644, 71

Komatsu E., Dunkley J., The WMAP Team, 2009, ApJS, 180, 330

Kratochvil J. M., Haiman Z., May M., 2010, Phys. Rev. D, 81, 043519

Kratochvil J. M., Lim E. A., Wang S., Haiman Z., May M., Huffenberger K., 2011, ArXiv e-prints

Kuijken K., 2010, in Block D. L., Freeman K. C., Puerari I., eds, Galaxies and Their Masks. Springer-Verlag, New York, p. 361

LSST Science Collaborations et al., 2009, ArXiv e-prints

Marian L., Bernstein G. M., 2006, Phys. Rev. D, 73, 123525

Marian L., Smith R. E., Bernstein G. M., 2009, ApJ, 698, L33

Marian L., Smith R. E., Bernstein G. M., 2010, ApJ, 709, 286

Marian L., Hilbert S., Smith R. E., Schneider P., Desjacques V., 2011, ApJ, 728, L13

Maturi M., Meneghetti M., Bartelmann M., Dolag K., Moscardini L., 2005, A&A, 442, 851

Maturi M., Angrick C., Pace F., Bartelmann M., 2010, A&A, 519, A23

Metzler C. A., White M., Loken C., 2001, ApJ, 547, 560

Navarro J. F., Frenk C. S., White S. D. M., 1997, ApJ, 490, 493

Okabe N., Takada M., Umetsu K., Futamase T., Smith G. P., 2010, PASJ, 62, 811

Pires S., Starck J.-L., Amara A., Réfrégier A., Teyssier R., 2009, A&A, 505, 969

Schirmer M., Erben T., Hetterscheidt M., Schneider P., 2007, A&A, 462, 875

Schneider P., 1996, MNRAS, 283, 837

Schneider P., van Waerbeke L., Jain B., Kruse G., 1998, MNRAS, 296, 873

Scoccimarro R., 1998, MNRAS, 299, 1097

Seljak U., Zaldarriaga M., 1996, ApJ, 469, 437

Semboloni E. et al., 2006, A&A, 452, 51

Sheth R. K., Tormen G., 1999, MNRAS, 308, 119

Smith R. E., 2009, MNRAS, 400, 851

Smith R. E., Marian L., 2011, MNRAS, 418, 729

Smith R. E., Watts P. I. R., 2005, MNRAS, 360, 203

Springel V., 2005, MNRAS, 364, 1105

Tang J. Y., Fan Z. H., 2005, ApJ, 635, 60

Tegmark M., Taylor A. N., Heavens A. F., 1997, ApJ, 480, 22

The Dark Energy Survey Collaboration, 2005, preprint (astro-ph/0510346)

The Euclid Collaboration, 2011, preprint (arXiv:1110.3193)

Wang S., Khoury J., Haiman Z., May M., 2004, Phys. Rev. D, 70, 123008

Yang X., Kratochvil J. M., Wang S., Lim E. A., Haiman Z., May M., 2011, Phys. Rev. D, 84, 043529

APPENDIX A: THE CORRELATION COEFFICIENT OF THE PEAK COUNTS

For a covariance matrix $\mathbf{C}$, the correlation coefficient is defined by

$$r_{ij} = \frac{C_{ij}}{\sqrt{C_{ii} C_{jj}}}. \tag{A1}$$

We explore the correlation coefficient of the peak abundance based on measurements from 128 fields of the fiducial model. Fig. A1 shows r for the hierarchical method, using aperture-mass bins. The mass is assigned according to the description given in Section 3. The result is very similar to the correlation coefficient of the 3D halo abundance (Smith & Marian 2011): there are strong correlations at the low-mass end ($M < 3 \times 10^{14}\, h^{-1}\, \mathrm{M}_\odot$) while the large-mass bins are mostly uncorrelated. In Fig. A2 we show the hierarchical results for r based on the same measurements, but using bins in S/N instead of mass. The same pattern as in the previous figure is visible, with the lower bins S/N ≤ 6 having a correlation coefficient of $\sim$0.4. Finally, Fig. A3 depicts r measured from the same fiducial maps, using a single filter of size $M = 2 \times 10^{15}\, h^{-1}\, \mathrm{M}_\odot$. The correlations seem weaker than for the hierarchical case, but they extend to higher S/N, the highest bin being however largely uncorrelated. This is further explained in the next figure.
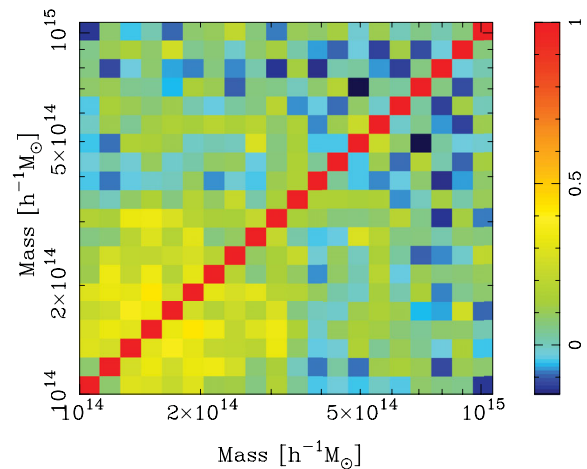

Figure A1. The correlation coefficient r_{ij} for the hierarchical peak abundance, binned in mass. The measurements are an average of 128 fields of the fiducial model.
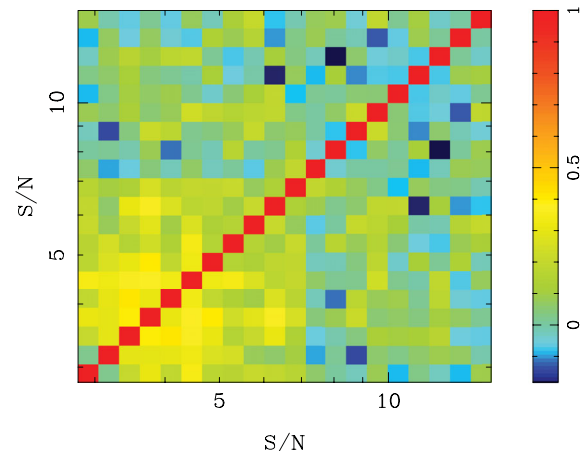

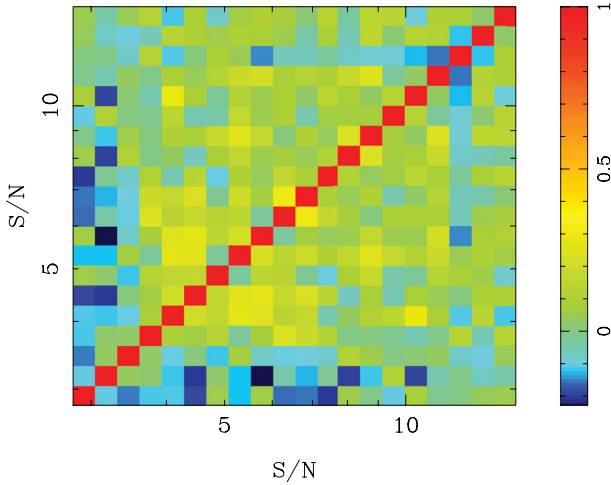**Figure A2.** Same as in the previous figure, only the binning is in S/N.

Figure A3. The correlation coefficient for the fiducial peak abundance measured with a filter of fixed size $M = 2 \times 10^{15}\,h^{-1}\,\mathrm{M}_\odot$. The binning is in S/N.
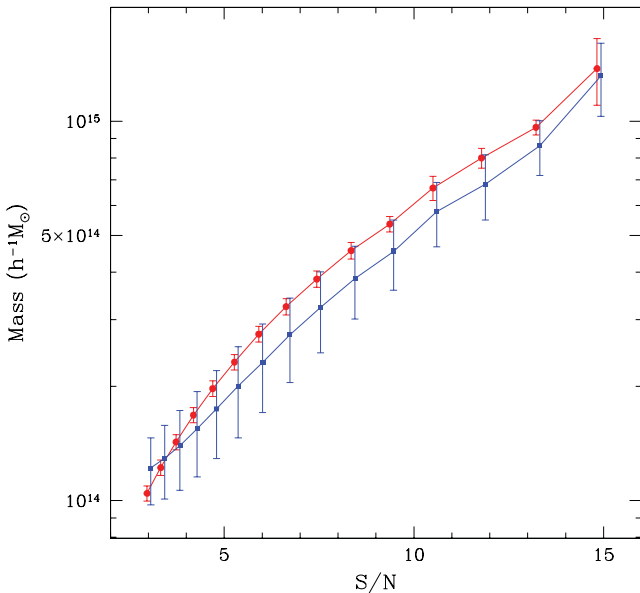

Figure A4. The S/N–mass relation for the hierarchical (red solid circles) and single-sized filtering methods (blue solid squares). For the latter, we adopted the size $M = 2 \times 10^{15}\,h^{-1}\,\mathrm{M}_\odot$. Only peaks detected through both methods are being compared. For both methods, the mass is *the hierarchical aperture mass* of equation (13). For the hierarchical method the relationship between the assigned mass and S/N of the peaks is very tight, with little scatter. For the single-sized method there is significantly more scatter, particularly for the lower S/N bins. For clarity, we have slightly offset the position of the points on the $\hat{\mathbf{x}}$-axis.

Fig. A4 presents the S/N–mass scatter of peaks detected through the two methods. For the fiducial-cosmology peak abundances, we compare the coordinates of the peaks to select only those peaks found through both methods. For these peaks, we concentrate on the following three quantities: the hierarchical S/N given by equa-

tion (14), the single-sized S/N from equation (7) and the hierarchical aperture mass from equation (13). We consider S/N bins. For each bin we compute the mean S/N of the hierarchical and single-sized peaks in that respective bin, as well as the mean mass, and the error on the mass. We emphasize that for both methods, by *mass* we mean the aperture mass assigned through the hierarchical algorithm, i.e. equation (13). The figure shows that both methods yield on average a similar relation between mass and S/N. However, in the hierarchical case, this relation is very tight: large-/small-mass peaks have large/small S/N, hence the similarity between the correlation matrices in Figs A1 and A2. For the single-filter method this is not the case, as the size of the error bars suggests that peaks with quite varying mass are binned in the same S/N bin. This is consistent with the correlation matrix shown in Fig. A3.

In Fig. A5 we compare the fractional cumulative errors obtained using the full covariance matrix equation (27) to the Poisson errors equation (28), for the two methods considered. The Poisson and full covariance errors converge at the high-S/N end, in accord with the fact that the most massive peaks are assigned the largest S/N in both the hierarchical and single-filter methods. Finally, in Fig. A6 we show the fractional and cumulative Fisher errors for the hierarchical method, considering binning in mass, and not S/N. As already suggested by Fig. A1, the Poisson statistic captures reasonably well the high-mass end of the distribution of hierarchical peaks, where the full covariance and Poisson errors converge.

To conclude, the Poisson distribution *can* be used to approximate the likelihood function of high-S/N and high-mass hierarchical peaks.

APPENDIX B: THE NUMBER OF BINS

We now address the issue of the number of bins used to estimate the Fisher matrix in equation (27). We expect that too coarse a binning will diminish the constraints, as the information in the maps would not be fully captured. We also expect the constraints to saturate once a large enough number of bins is considered. However, for all filtering methods we noticed a continuous improvement in the constraints with the increasing number of bins. This is most likely due to noise in the covariance matrix measurement.

As a remedy, we apply the correction discussed by Hartlap, Simon & Schneider (2007). Given a data set drawn from a multivariate Gaussian distribution, and given the maximum-likelihood estimator for the covariance matrix $\mathbf{C}$, i.e. equation (30), then an unbiased estimator for the inverse covariance is

$$\widehat{\mathbf{C}^{-1}} = \frac{N - N_{\mathrm{bin}} - 2}{N - 1}(\hat{\mathbf{C}})^{-1}, \quad N_{\mathrm{bin}} < N - 2, \tag{B1}$$

where N_{bin} is the number of bins, and N is the number of realizations – in our case the number of fiducial fields. We use logarithmically spaced S/N bins in the interval [2.8, 14]. Estimating our Fisher matrix with the above equation alleviated significantly the dependence of the constraints on the number of bins used, as seen in Fig. B1. The figure shows the dependence of the unmarginalized Fisher errors on the number of bins in which the S/N interval is divided. All errors show little evolution with the number of bins, and are relatively stable once $N_{\mathrm{bin}} \sim 20$, except for the case of n_{s}, where there is slightly more evolution. The entire analysis presented in this work was carried out for $N_{\mathrm{bin}} = 20$.
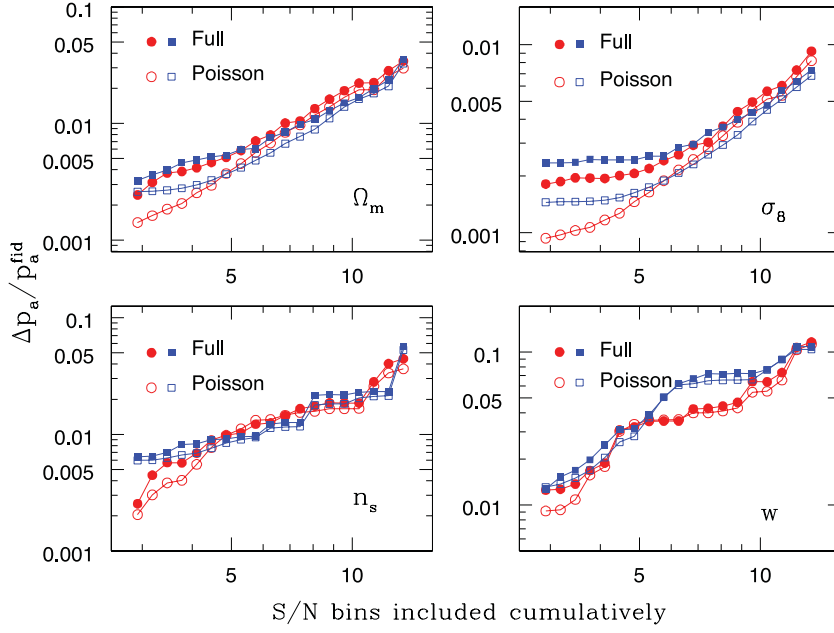
Figure A5. Comparison between Poisson and full covariance fractional unmarginalized errors, i.e. equations (28) and (27). For clarity, we show only the results for a single-sized filter of $M = 2 \times 10^{15}\, h^{-1}\, M_\odot$ – blue squares – and the hierarchical method – red circles. The full errors are the same as in Fig. 5.
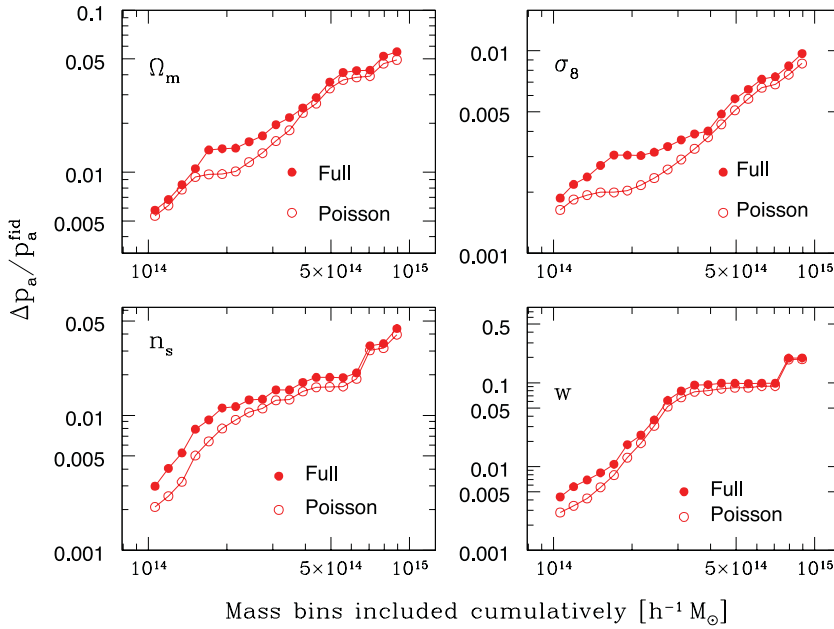

Figure A6. Comparison between the full covariance and Poisson cumulative unmarginalized errors, with the information binned in terms of aperture mass, i.e. equation (13). We show only results for the hierarchical method. The two errors converge at the high-mass end, so the hierarchical algorithm successfully assigns the highest masses to the most massive peaks, well described by the Poisson distribution. These results are similar to those shown in Fig. A5.
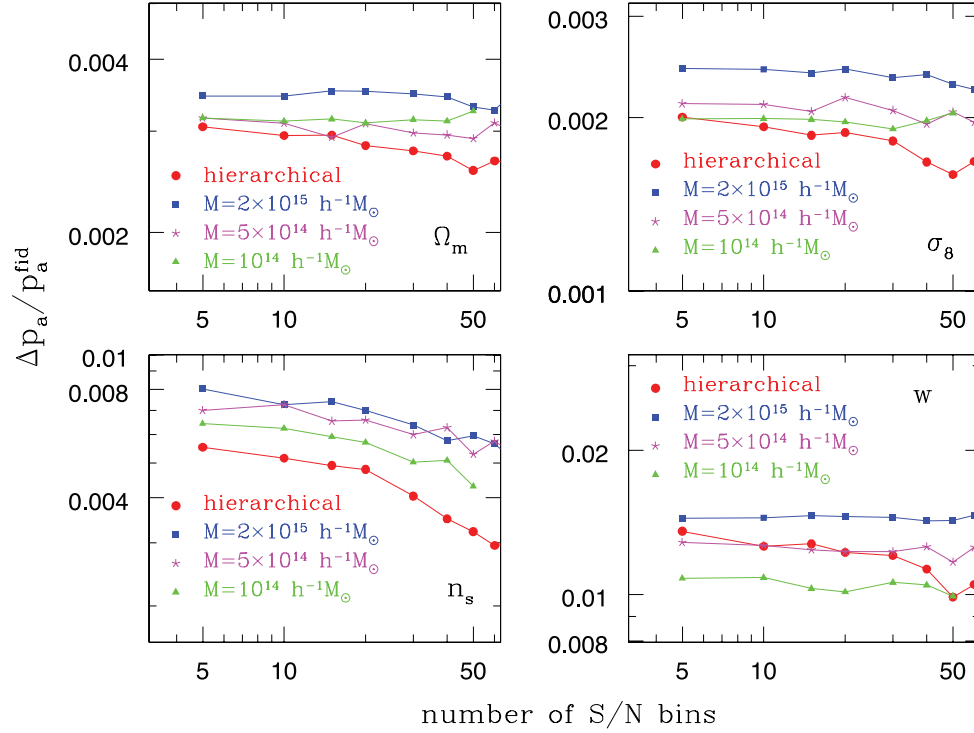
Figure B1. Dependence of the fractional unmarginalized errors on the number of S/N bins. We used equation (B1) to estimate the Fisher matrix equation (27). The hierarchical method performs best for a choice of $N_{\text{bin}} = 20$, while the single-filtering results seem largely independent of the number of bins used.

This paper has been typeset from a TEX/LATEX file prepared by the author.